Polarization of Molecules Induced by Intense Nonresonant Laser Fields

ARTICLE *in* THE JOURNAL OF PHYSICAL CHEMISTRY · OCTOBER 1995

Impact Factor: 2.78 · DOI: 10.1021/j100042a051

2 AUTHORS:

Bretislav Friedrich
Fritz Haber Institute of the Max Planck Society
144 PUBLICATIONS **4,714** CITATIONS

SEE PROFILE

Dudley R Herschbach
Harvard University
136 PUBLICATIONS **4,490** CITATIONS

SEE PROFILE

Polarization of Molecules Induced by Intense Nonresonant Laser Fields

Bretislav Friedrich* and Dudley Herschbach*

Department of Chemistry, Harvard University, 12 Oxford Street, Cambridge, Massachusetts 02138

Received: June 28, 1995; In Final Form: August 24, 1995[⊗]

The anisotropic interaction of the electric field vector of intense laser radiation with the dipole moment *induced* in a *polarizable* molecule by the laser field creates aligned pendular states. These are directional superpositions of field-free states, governed by a $\cos^2\theta$ potential (with θ the angle between the molecular axis and the field vector). We show that the spatial alignment and other eigenproperties can be derived from spheroidal wave functions, give explicit expressions for low- and high-field limits, contrast the induced pendular states with those for permanent dipoles subject to static fields, and present calculations demonstrating the utility of the induced states for rotational spectroscopy, laser alignment, and spatial trapping of molecules.

1. Introduction

When subject to an external electric field, the electronic distribution of any molecule (or atom) is distorted to some extent. This interaction, governed by the molecular polarizability, results in an induced dipole moment. For experimentally feasible static fields, such induced moments are very weak, typically only on the order of 10^{-2} D units.[1] However, far stronger induced moments, well above 1 D, can now be produced by intense laser fields, using either pulsed lasers or supermirror techniques to build up a CW laser mode. This makes it possible to study nonpolar molecules by means that otherwise require permanent dipole moments. The polarizability interaction with an intense nonresonant laser field can be exploited to extend rotational spectroscopy to nonpolar molecules, to suppress rotational tumbling and thereby align the internuclear axis (as in kindred work with permanent dipoles[2,3]), or to attain spatial trapping of molecules.[4]

The polarizability interaction is governed by a $\cos^2\theta$ potential, in contrast to a $\cos\theta$ potential for a permanent dipole (with θ the angle between the molecular axis and the electric field direction). If the field is sufficiently strong, these anisotropic interactions create pendular states, directional superpositions of the field-free rotational states in which the molecular axis librates about the field direction. In section 2, we evaluate the pendular energy levels and wave functions for the $\cos^2\theta$ potential in terms of the well-known spheroidal functions.[4,5] As this is a double-well potential, with end-for-end symmetry, the levels exhibit characteristic tunnel-effect splittings. We also examine correlations with the field-free rotor states and the high-field harmonic librator limit. In section 3, we compare level patterns, torques, and angular momentum transfer with those for the permanent dipole case. In section 4, we determine the angular distribution of the molecular alignment, characterized by $\langle\cos^2\theta\rangle$ and its ensemble average. Section 5 presents calculations for some representative molecules and prospective applications.

2. Pendular Eigenstates for an Induced Dipole

For simplicity, we consider a linear rotor subject to plane-wave radiation with electric field strength $\epsilon = \epsilon_0 \cos(2\pi\nu t)$. The Schrödinger equation is

$$[BJ^2 + V_\mu(\theta) + V_\alpha(\theta)]\Psi = E\Psi \tag{1}$$

with J^2 the squared angular momentum operator, B the rotational constant, E the eigenenergy, and θ the polar angle between the molecular axis and the electric field direction. For a permanent dipole moment μ along the internuclear axis and polarizability components $\alpha_\parallel$ and $\alpha_\perp$ parallel and perpendicular to the axis, the interaction potentials are

$$V_\mu(\theta) = -\mu\epsilon\cos\theta \tag{2a}$$

$$V_\alpha(\theta) = -{}^1/_2\epsilon^2(\alpha_\parallel\cos^2\theta + \alpha_\perp\sin^2\theta) \tag{2b}$$

For nonresonant frequencies much greater than the reciprocal of the laser pulse duration, $\nu \gg \tau_p^{-1}$, averaging over the pulse period τ_p quenches the V_μ interaction and converts ϵ^2 in V_α to $\epsilon_0^2/2$. The time average of the Hamiltonian thus becomes

$$H = BJ^2 + \bar{V}_\alpha = BJ^2 - {}^1/_4\epsilon_0^2[(\alpha_\parallel - \alpha_\perp)\cos^2\theta + \alpha_\perp] \tag{3}$$

The same form holds for a nonpolar molecule subject to a static field of strength $\epsilon_0/2^{1/2}$.

Spheroidal Wave Equation. The Schrödinger equation obtained from eq 3 reduces to a spheroidal wave equation,

$$\left[\frac{d}{dz}\left[(1-z^2)\frac{d}{dz}\right] - \frac{M^2}{1-z^2} + \lambda_{J,M} + c^2z^2\right]S_{J,M} = 0 \tag{4}$$

where $z = \cos\theta$. This simple reduction apparently has only recently been noted.[4] The quantity c^2, a dimensionless anisotropy parameter, is given by

$$c^2 \equiv \Delta\omega = \omega_\parallel - \omega_\perp = (\alpha_\parallel/\alpha_\perp - 1)\omega_\perp \tag{5}$$

where

$$\omega_{\parallel,\perp} \equiv [\alpha_{\parallel,\perp}\epsilon_0^2/(4B)] \tag{6}$$

When $\alpha_\parallel > \alpha_\perp$, which always holds for linear molecules, $\Delta\omega > 0$; this corresponds to the *oblate* spheroidal case. When $\alpha_\parallel < \alpha_\perp$, which occurs for some planar molecules such as benzene, $\Delta\omega < 0$; this corresponds to the *prolate* spheroidal case, which we consider also because it provides instructive contrasts. As seen in Figure 1, for the oblate case V_α is a double-well potential, with minima at $\theta = 0°$ and 180°, whereas for the prolate case V_α has a single minimum at $\theta = 90°$.

The separation constant, $\lambda_{J,M}$, and eigenfunctions, $S_{J,M}$, can be obtained from extensive tabulations or computed with arbitrary accuracy by standard methods.[5,6] The separation constants are related to the eigenenergies by

$$\lambda_{J,|M|} = \omega_\perp + E_{J,|M|}/B \tag{7}$$

[⊗] Abstract published in *Advance ACS Abstracts,* October 1, 1995.

0022-3654/95/2099-15686$09.00/0

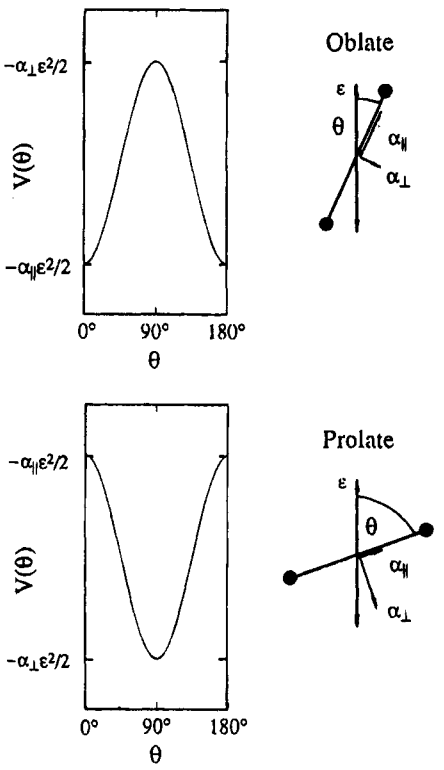

Figure 1. Contrast of optimal alignments for oblate and prolate versions of anisotropic polarizability interaction, governed by eq 3. For the oblate case, the pair of potential minima in the polar regions, $\theta = 0°$ and 180°, are separated by an equatorial barrier that hinders end-for-end rotation via $\theta \rightarrow \pi - \theta$. For the prolate case, the potential minimum at $\theta = 90°$ extends around the equator, so does not restrain end-for-end rotation via the azimuthal angle $\varphi \rightarrow \varphi + \pi$.

and the Schrödinger eigenfunctions are given by

$$\Psi = S_{\tilde{J},|M|}e^{i|M|\varphi} \equiv |\tilde{J},|M|;\Delta\omega\rangle \qquad (8)$$

with φ the azimuthal angle. The eigenfunctions can be conveniently expanded in spherical harmonics,

$$|\tilde{J},|M|;\Delta\omega\rangle = \sum_{J=2n}^{\infty} d_{J,M}(\Delta\omega)Y_{J,|M|}(\theta,\varphi) \quad \text{for } \tilde{J} \text{ even} \quad (9)$$

$$= \sum_{J=2n+1}^{\infty} d_{J,M}(\Delta\omega)Y_{J,|M|}(\theta,\varphi) \quad \text{for } \tilde{J} \text{ odd}$$

Here $2n = m + |M|$ and $2n + 1 = m + |M|$ with m either 0, 2, 4, ... or 1, 3, 5, ... The expansion coefficients, $d_{J,M}(\Delta\omega)$, depend solely on the interaction parameter $\Delta\omega$. For any fixed value of the good quantum number M, the range of J involved in this coherent superposition or hybrid wave function increases with the $\Delta\omega$ parameter. Since the hybrid wave functions comprise either even or odd J's, each state is of a definite parity, $(-1)^{\tilde{J}}$.

For $\Delta\omega = 0$, the eigenproperties become those of a field-free rotor; the eigenfunctions then coincide with spherical harmonics, and the eigenvalues become $\lambda_{\tilde{J},|M|} \rightarrow E_{J,|M|}/B = J(J + 1)$. The eigenstates can thus be labeled by $|M|$ and the nominal value $\tilde{J}$, designating the angular momentum for the field-free rotor state that adiabatically correlates with the high-field hybrid function.

In the high-field limit, $\Delta\omega \rightarrow \infty$, the range of θ is confined near the potential minimum and eq 4 reduces to that for a two-dimensional angular harmonic librator. Note that in the oblate case, states with $\tilde{J} = N + 1$ for $\tilde{J} - |M|$ odd and $\tilde{J} = |N|$ for $\tilde{J} - |M|$ even, with the same $N = 2(k + |M|/2)$ and $k = 0, 1, 2, ...$, have equal energies in the harmonic librator limit. In the prolate case, states with the same $\tilde{J} - |M|$ have the same harmonic energies.

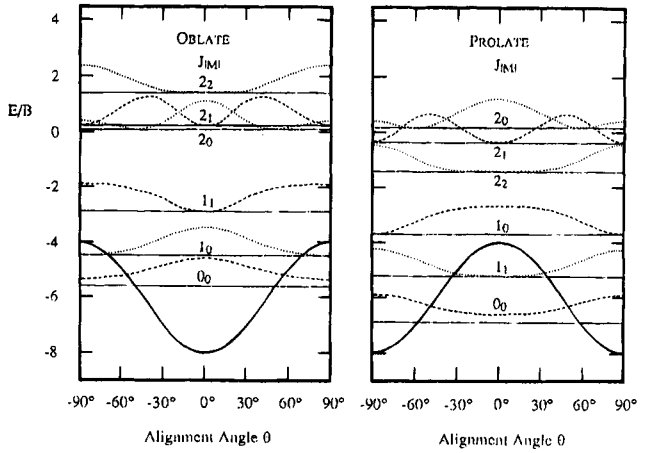

Figure 2. Potential energy (bold full lines), energy levels (full lines) in units of the rotational constant B, and squares of spheroidal wave functions (dashed lines) for $|\Delta\omega| = 4$. The oblate case (at left) has $\alpha_\parallel/\alpha_\perp = 2$; the prolate case (at right) has $\alpha_\parallel/\alpha_\perp = 1/2$. For both oblate and prolate cases, the interaction potentials have $V(0°)/B = \omega_\parallel$ and $V(90°)/B = \omega_\perp$. All levels are shifted toward negative energies with respect to the free rotor ground state by $\omega_\perp$. Although the physical range of the angle θ is $0° \leftrightarrow 180°$, here the $-90° \leftrightarrow 90°$ range is plotted to better display the oblate state wave functions. See text, eqs 3–6.

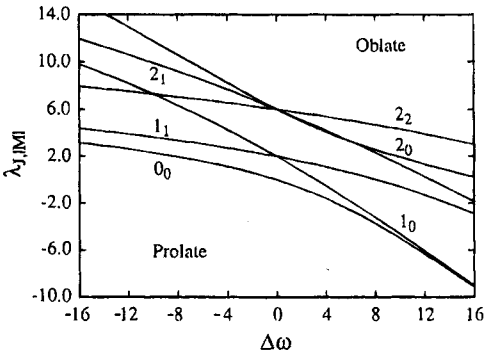

Figure 3. Dependence of the spheroidal separation constant $\lambda_{\tilde{J},|M|}$ of eq 4 on the anisotropy parameter $\Delta\omega$ for the lowest six pendular states. See eq 7 for relation to energy levels. For the oblate case, $\Delta\omega$ is positive; for the prolate case, negative.

Eigenproperties. Figure 2 shows the interaction potential, $-(\omega_\perp + \Delta\omega\cos^2\theta)$, the energy levels, and the squares of the spheroidal wave functions $S_{\tilde{J},|M|}$ for typical values of the polarizability anisotropy: $\alpha_\parallel/\alpha_\perp = 2$ (oblate), $\alpha_\parallel/\alpha_\perp = 1/2$ (prolate), but for simplicity, a low value for the reduced parameter $|\Delta\omega| = 4$. The potential is purely attractive. The $\omega_\perp$ term contributes a uniform shift toward negative energies; the $\Delta\omega$ term governs the amplitude and location of the potential wells. The number of bound states thus increases with $|\Delta\omega|$, *i.e.* grows quadratically with field strength.

Figures 3 and 4 display, for the lowest six pendular states, the dependence on $\Delta\omega$ of the eigenvalues, $\lambda_{\tilde{J},|M|}$, and the expectation values of the squared alignment cosine, $\langle\cos^2\theta\rangle_{\tilde{J},|M|}$. The latter is readily evaluated via the Hellmann–Feynman theorem,

$$\langle\cos^2\theta\rangle_{\tilde{J},|M|} = -\partial(E_{\tilde{J},|M|}/B)/\partial(\Delta\omega) \qquad (10)$$

The energy levels decrease with increasing field strength for the oblate case, whereas they increase for the prolate case. This

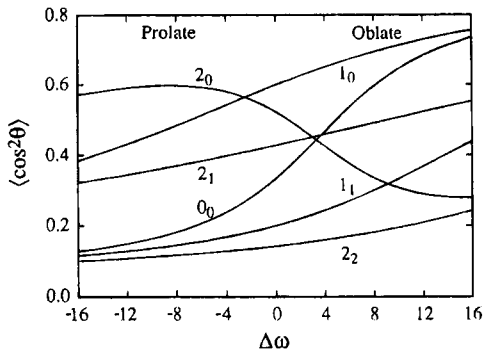

Figure 4. Dependence of the alignment parameter $\langle\cos^2\theta\rangle_{\tilde{J},|M|}$ of eq 10 on $\Delta\omega$ for the lowest six pendular states; *cf.* Figure 3.

reflects directly the opposite sense of the polarizability anisotropy, depicted in Figure 1. Likewise, $\langle\cos^2\theta\rangle$ increases with $\Delta\omega$ for the oblate case because the induced dipole moment is parallel to the molecular axis, whereas $\langle\cos^2\theta\rangle$ decreases with increasing $|\Delta\omega|$ for the prolate case because the induced dipole is perpendicular to the figure axis.

Table 1 gives the leading terms in perturbation expansions for the eigenenergy $E_{\tilde{J},|M|}$ and for $\langle\cos^2\theta\rangle_{\tilde{J},|M|}$ applicable when $|\Delta\omega|$ is small or large, corresponding to the low- and high-field limits.

Effective Potentials. For any system treated in curvilinear coordinates, the nonuniform spatial weighting introduced by the Jacobian factor must be taken into account. This may be done in the usual way[7] by transforming to a probability amplitude Φ with unit Jacobian, $|\Phi|^2 = |\Psi|^2 \sin\theta$. The corresponding Hamiltonian then takes the form

$$H = -B\frac{d^2}{d\theta^2} + V_{\text{eff}}(\theta) \tag{11}$$

which describes one-dimensional motion in the polar angle θ, subject to an effective potential

$$V_{\text{eff}}(\theta) = B\left[\frac{|M|^2 - \frac{1}{4}}{\sin^2\theta} - \frac{1}{4}\right] + \bar{V}_\alpha \tag{12}$$

This displays explicitly the role of the M-dependent centrifugal term, which for $|M| > 0$ provides a repulsive contribution competing with the attractive polarizability interaction.

Figures 5 and 6 plot for the oblate and prolate case, respectively, the effective potentials and energy levels, for $|M| = 0-5$ and $|\Delta\omega| = 49$. For the oblate case, if $M^2 - {}^1/_4 < \Delta\omega$, the effective potential exhibits a double well with an equatorial barrier. At the barrier maximum, $V_{\text{eff}}(90°)/B = M^2 - {}^1/_2 - \omega_\perp$. The two equivalent potential minima occur at θ_m, given by

$$\sin\theta_m = \left[\left(M^2 - \frac{1}{4}\right)/(\Delta\omega)\right]^{1/4} \tag{13}$$

and there $V(\theta_m)/B = -\Delta\omega\cos 2\theta_m - {}^1/_4 - \omega_\perp$. The barrier height is thus $\Delta V/B = \Delta\omega(1 - \sin^2\theta_m)^2$. For the prolate-case, V_{eff} has a single minimum flanked by barriers in the polar regions. This determines the angular ranges accessible to the librating/pinwheeling molecular axis. For both the oblate and prolate cases, the energy levels conform to $E_{\tilde{J},|M|} < E_{\tilde{J}+1,|M|+1}$ and $E_{\tilde{J},|M|} < E_{\tilde{J}+1,|M|+1}$. However, the ordering of levels with the same $\tilde{J}$ but different $|M|$ is distinctive. In the prolate case, $E_{\tilde{J},|M|+1} < E_{\tilde{J},|M|}$. This occurs because states aligned perpendicular to the field have the lowest energy and as $|M|$ increases, the effective potential increasingly restricts the angular range about $\theta = 90°$. In the oblate case, $E_{\tilde{J},|M|+1} > E_{\tilde{J},|M|}$. There the energy is lowest for states aligned along the field but as $|M|$ increases, V_{eff} increasingly excludes angles close to 0° and 180°.

For the oblate case, in the double-well regime each $|M|$ manifold exhibits the pairing of levels associated with tunneling between the equivalent minima at 0° and 180°. Figure 7 plots the eigenvalue differences between the paired levels as functions of $\Delta\omega^{1/2}$. The splittings diminish exponentially, and the logarithmic slope is nearly independent of $|M|$.

Also indicated in Figures 5 and 6, by pairs of dots on each energy level, are the angular amplitudes corresponding to the

TABLE 1: Linear Molecule with Induced Dipole Moment: Limiting Values of Eigenenergy and Axis Alignment[a]

	$E_{\tilde{J},M}/B$	$\langle\cos^2\theta\rangle$
	Oblate	
low field: $\Delta\omega \to 0$	$\tilde{J}(\tilde{J}+1) - \frac{\Delta\omega}{2}\left[1 - \frac{(2\lvert M\rvert - 1)(2\lvert M\rvert + 1)}{(\tilde{J}-1)(2\tilde{J}+3)}\right] - \omega_\perp$	$\frac{1}{2}\left[1 - \frac{(2\lvert M\rvert - 1)(2\lvert M\rvert + 1)}{(2\tilde{J}-1)(2\tilde{J}+3)}\right] + \Delta\omega\left[\frac{(\tilde{J} - \lvert M\rvert + 1)(\tilde{J} - \lvert M\rvert + 2)(\tilde{J} + \lvert M\rvert + 1)(\tilde{J} + \lvert M\rvert + 2)}{2(2\tilde{J}+1)(2\tilde{J}+3)^3(2\tilde{J}+5)}\right]$
high field: $\Delta\omega \to \infty$	$-\Delta\omega - \omega_\perp + 2(\Delta\omega)^{1/2} + 2(\Delta\omega)^{1/2}\tilde{J} + \lvert M\rvert^2/2 - \tilde{J}^2/2 - \tilde{J} - 1$	$1 - \frac{\tilde{J}+1}{(\Delta\omega)^{1/2}}$ for $(\tilde{J} - \lvert M\rvert)$ even
	$-\Delta\omega - \omega_\perp + 2(\Delta\omega)^{1/2}\tilde{J} + \lvert M\rvert^2/2 - \tilde{J}^2/2 - 1/2$	$1 - \frac{\tilde{J}}{(\Delta\omega)^{1/2}}$ for $(\tilde{J} - \lvert M\rvert)$ odd
	Prolate	
low field: $\Delta\omega \to 0$	$\tilde{J}(\tilde{J}+1) + \frac{\Delta\omega}{2}\left[1 - \frac{(2\lvert M\rvert - 1)(2\lvert M\rvert + 1)}{(2\tilde{J}-1)(2\tilde{J}+3)}\right] - \omega_\perp$	$\frac{1}{2}\left[1 - \frac{(2\lvert M\rvert - 1)(2\lvert M\rvert + 1)}{(2J-1)(2J+3)}\right] - \Delta\omega\left[\frac{(J - \lvert M\rvert + 1)(J - \lvert M\rvert + 2)(J + \lvert M\rvert + 1)(J + \lvert M\rvert + 2)}{2(2J+1)(2J+3)^3(2J+5)}\right]$
high field: $\Delta\omega \to \infty$	$2\Delta\omega^{1/2}(\tilde{J} - \lvert M\rvert + 1) + \lvert M\rvert^2 - \frac{1}{8}\{[2(\tilde{J} - \lvert M\rvert) + 1]^2 + 5\} - \frac{2(\tilde{J} - \lvert M\rvert) + 1}{64\Delta\omega^{1/2}}\{[2(\tilde{J} - \lvert M\rvert) + 1]^2 + 11 - 32\lvert M\rvert^2\} - \omega_\perp$	$-\frac{[2(\tilde{J} - \lvert M\rvert) + 1] + \{[2(\tilde{J} - \lvert M\rvert) + 1]^2 - 32\lvert M\rvert^2\}}{128\Delta\omega^{3/2}} - \frac{\tilde{J} - \lvert M\rvert + 1}{\Delta\omega^{1/2}}$

[a] $\Delta\omega \rangle \omega_\parallel - \omega_\perp$, with $\omega_{\parallel,\perp} \equiv [\alpha_{\parallel,\perp}\epsilon^2/2B] = [\alpha_{\parallel,\perp}\epsilon_0{}^2/4B]$.

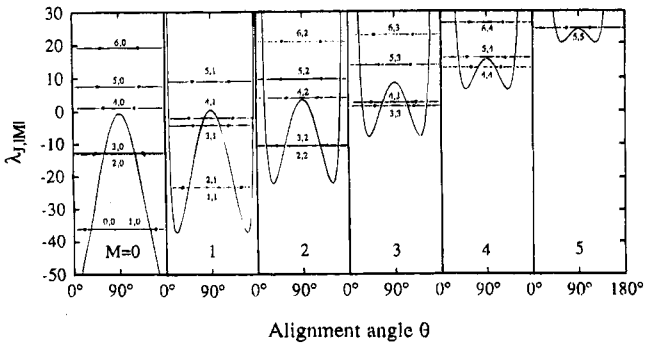

Figure 5. Effective potentials (bold lines, eq 12), separation constants (full lines, eq 7), and alignment angular amplitude $\theta_\pm$ (dots), sorted according to values of $|M|$ for the *oblate* case with $\Delta\omega = 49$. Eigenstates are labeled by $\tilde{J},|M|$.

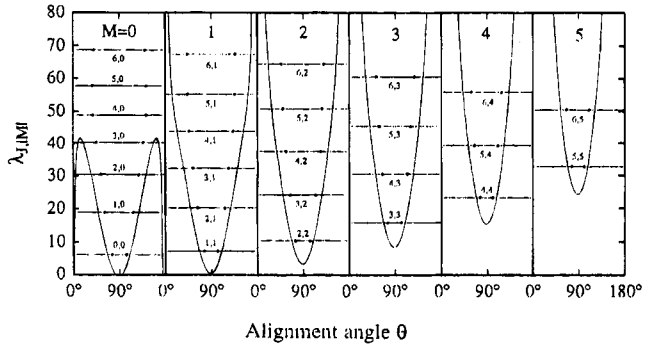

Figure 6. Effective potentials (bold lines), separation constants (full lines), and alignment angular amplitude $\theta_\pm$ (dots), sorted according to values of $|M|$ for the *prolate* case with $\Delta\omega = -49$. Eigenstates are labeled by $\tilde{J},|M|$.

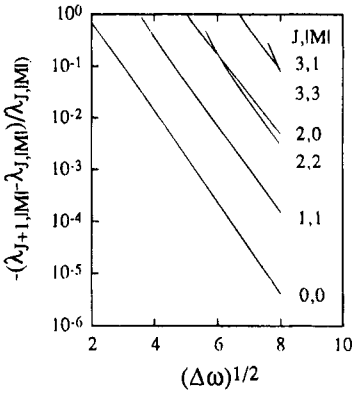

Figure 7. Energy splittings of bound states for the oblate case, corresponding to Figure 5. Data are from tables of ref 6.

expectation values of the squared cosine, defined by $\theta_\pm \equiv \arccos\sqrt{\langle\cos^2\theta\rangle}$. For a given $\Delta\omega$ and $|M|$, as $\tilde{J}$ increases, $\langle\cos^2\theta\rangle$ retreats from its high-field limit towards its field-free value, *cf.* Table 1: for $|M| < \tilde{J}$, $\langle\cos^2\theta\rangle \to 1/2$ ($\theta_\pm \to 45°$), whereas for $|M| = \tilde{J}$, $\langle\cos^2\theta\rangle \to 0$ ($\theta_\pm \to 90°$).

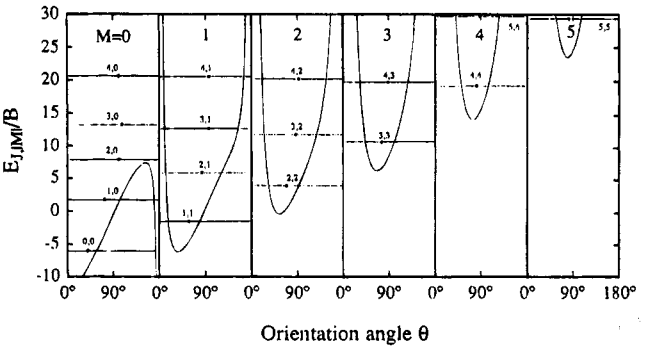

Figure 8. Effective potentials (bold lines), separation constants (full lines), and nominal orientation angle θ_μ (dots) sorted according to values of $|M|$ for the *permanent dipole* case with $\omega = 10$. States are labeled by $\tilde{J},|M|$.

3. Induced and Permanent Dipole Interactions Compared

The eigenproperties of a permanent dipole μ subject to a *static* electric field F have been extensively treated.[8] Table 2 gives the low- and high-field limits for the energy levels and the orientation cosine, $\langle\cos^2\theta\rangle$, in terms of the dimensionless interaction parameter $\omega_\mu \equiv \mu F/B$. When recast to have a unit Jacobian, the Hamiltonian has the same form as eq 11, with V_α replaced by $V_\mu = -\mu F\cos\theta$ in the effective potential. Figure 8 plots V_{eff} for $\omega = 10$ and $|M| = 0-5$ together with the energy levels and orientation angle $\theta_\mu \equiv \arccos\langle\cos\theta\rangle$. In contrast to Figures 5 and 6, the effective potential for a permanent dipole is asymmetric about 90°, disfavoring angles near 180°, and increasingly so with increasing $|M|$. Since the energy is lowest when the dipole is oriented along the field, for any given $\tilde{J}$ the eigenenergies increase with decreasing $|M|$. Within each $|M|$ manifold, the best orientation, *i.e.*, with θ_μ closest to 0°, is attained for $\tilde{J} = |M|$.

Other distinctive aspects of permanent and induced dipoles are exemplified in the torque exerted on the dipole by an imposed field and the associated change in angular momentum. The torque is given by

$$\mathrm{d}|\bar{\mathbf{J}}|/\mathrm{d}t = -\mathrm{d}V_\alpha/\mathrm{d}\theta \tag{14}$$

Since the angular velocity is $\mathrm{d}\theta/\mathrm{d}t = |\mathbf{J}|/I$, where $I = \hbar^2/2B$ is the moment of inertia of the rotor, eq 14 yields the Ehrenfest theorem[9] in the form

$$I\frac{\mathrm{d}^2}{\mathrm{d}t^2}\langle\theta\rangle = I\langle\ddot{\theta}\rangle = -\left\langle\frac{\mathrm{d}V_\alpha}{\mathrm{d}\theta}\right\rangle \tag{15}$$

For an induced dipole, the expectation value of the torque is 0 for any state, as

$$-\langle\mathrm{d}V_\alpha/\mathrm{d}\theta\rangle = 2B\Delta\omega\langle\cos\theta\sin\theta\rangle = 0 \tag{16}$$

Thus, the average angular acceleration is 0, so even in the presence of an external field the average angular velocity is

TABLE 2: Linear Molecule with Permanent Dipole Moment: Limiting Values of Eigenenergy and Axis Orientation[a]

	$E_{\tilde{J},M}/B$	$\langle\cos\theta\rangle$
low field: $\omega \to 0$	$\tilde{J}(\tilde{J}+1) + \frac{\omega^2}{2}\left[\frac{\tilde{J}^2 - \lvert M\rvert^2}{\tilde{J}(2\tilde{J}+1)(2\tilde{J}-1)} - \frac{(\tilde{J}+1)^2 - \lvert M\rvert^2}{(\tilde{J}+1)(2\tilde{J}+1)(2\tilde{J}+3)}\right]$	$\omega\left[\frac{(\tilde{J}+1)^2 - \lvert M\rvert^2}{(\tilde{J}+1)(2\tilde{J}+1)(2\tilde{J}+3)} - \frac{\tilde{J}^2 - \lvert M\rvert^2}{\tilde{J}(\tilde{J}+1)(2\tilde{J}-1)}\right]$
high field: $\omega \to \infty$	$-\omega + (2\tilde{J} - \lvert M\rvert + 1)(2\omega)^{1/2}$	$1 - \frac{2\tilde{J} - \lvert M\rvert + 1}{(2\omega)^{1/2}}$

[a] $\omega \equiv \mu\epsilon/B$.

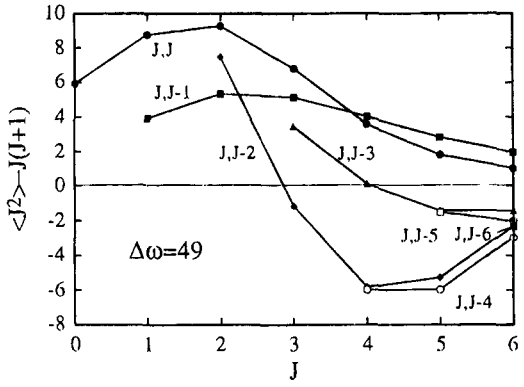

Figure 9. Net change of the expectation value of the squared angular momentum in the oblate case at $\Delta\omega = 49$ for states with $\tilde{J}$ and $|M|$ up to 6.

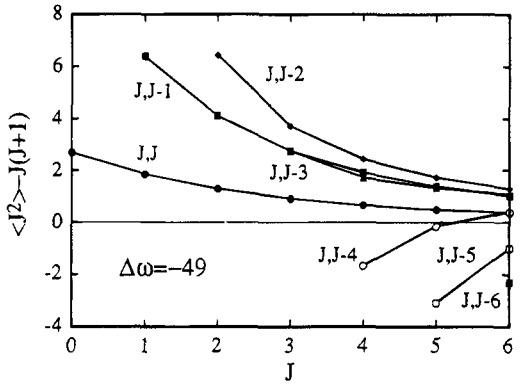

Figure 10. Net change of the expectation value of the squared angular momentum in the prolate case at $\Delta\omega = -49$ for states with $\tilde{J}$ and $|M|$ up to 6.

constant. For a permanent dipole, the expectation value of the torque and hence the angular acceleration is in general nonzero,

$$-\langle dV/d\theta\rangle = B\omega\langle\sin\theta\rangle \neq 0 \tag{17}$$

A related property is the change in the expectation value of the squared angular momentum with respect to the field-free case,

$$\langle\Delta\mathbf{J}^2\rangle_{\tilde{J},|M|} \equiv \langle\mathbf{J}^2\rangle_{\tilde{J},|M|} - \tilde{J}(\tilde{J}+1) \tag{18}$$

This quantity classifies the eigenstates according to whether they gain or lose angular momentum from the field. Since $B\langle\mathbf{J}^2\rangle = E_{\tilde{J},|M|} - \langle V\rangle$, expressions for $\langle\mathbf{J}^2\rangle$ in the high- and low-field limits are readily obtained from Tables 1 and 2. These suffice for a qualitative explication of the marked variations in the angular momentum transfer displayed in Figures 9−11. For an induced dipole, $\langle\mathbf{J}^2\rangle$ is always positive at the high-field limit, whereas it is negative at the low-field limit. The extent to which, for any specified $\Delta\omega$, a given state donates or accepts angular momentum from the field thus depends on how close it is to the high- or low-field limit. For a permanent dipole, $\langle\mathbf{J}^2\rangle$ is likewise positive at the high-field limit. However, $\langle\mathbf{J}^2\rangle$ can be either positive or negative at the low-field limit (*cf.* Table 2), depending on whether or not the state at a given ω is bound.

4. Alignment Angular Distribution

For an induced dipole in a given eigenstate, the absolute square of the spheroidal wave function, $|S_{\tilde{J},|M|}(\theta)|^2$, gives the distribution of the alignment of the molecular axis. However, what is usually needed is an ensemble average. Provided the field direction is essentially constant, $|M|$ remains an adiabatic quantum number. If changes in the field strength are also gradual enough, the initial population of the field-free rotational states will be adiabatically transformed into the spheroidal eigenstates. With Boltzmann weighting, the thermal average of the alignment distribution is then

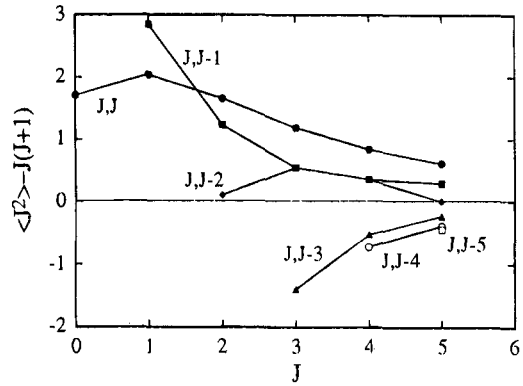

Figure 11. Net change of the expectation value of the squared angular momentum in the permanent dipole case at $\omega = 10$ for states with $\tilde{J}$ and $|M|$ up to 5.

$$\varrho(\theta) = \sum_{\tilde{J}} w_{\tilde{J}} \sum_{M=-\tilde{J}}^{M=+\tilde{J}} |S_{\tilde{J},|M|}|^2 \tag{19}$$

where

$$w_{\tilde{J}} = \frac{\exp[-\tilde{J}(\tilde{J}+1)\mathrm{Y}]}{Q_r} \tag{20}$$

with Q_r the rotational partition function and $\mathrm{Y} \equiv kT/B$ the reduced rotational temperature. It is customary to express the alignment angular distribution as a Legendre expansion,

$$\varrho(\theta) = 1 + \sum_n b_n P_n(\cos\theta) \tag{21}$$

where n is even. The coefficients are

$$b_n = (2n+1)\langle\langle P_n(\cos\theta)\rangle\rangle \tag{22}$$

where the ensemble average is given by

$$\langle\langle P_n(\cos\theta)\rangle\rangle = \sum_{\tilde{J}} w_{\tilde{J}} \sum_{M=-\tilde{J}}^{M=+\tilde{J}} \langle P_n(\cos\theta)\rangle_{\tilde{J},M} \tag{23}$$

with

$$\langle P_n(\cos\theta)\rangle_{\tilde{J},M} = \int_0^\pi |S_{\tilde{J},|M|}(\theta)|^2 P_n(\cos\theta)\, d(\cos\theta) \tag{24}$$

In particular, the second-order Legendre moment is

$$b_2(\Delta\omega,\mathrm{Y}) \equiv 5\langle\langle P_2(\cos\theta)\rangle\rangle = \frac{5}{2}(3\langle\langle\cos^2\theta\rangle\rangle - 1) \tag{25}$$

with

$$\langle\langle\cos^2\theta\rangle\rangle = \sum_{\tilde{J}} w_{\tilde{J}} \sum_{M=-\tilde{J}}^{M=+\tilde{J}} \langle\cos^2\theta\rangle_{\tilde{J},M} \tag{26}$$

This can be efficiently computed from the eigenvalues by means of the Hellmann−Feynman theorem, eq 10. In the low- and high-field limits, explicit expressions are readily evaluated from

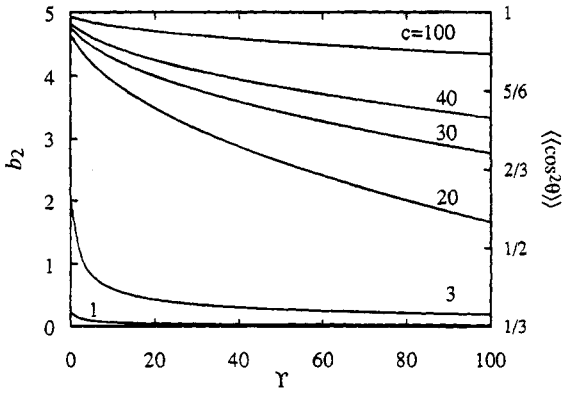

Figure 12. Dependence of ensemble-averaged alignment parameters b_2 and $\langle\langle\cos^2\theta\rangle\rangle$ of eqs 25 and 26 on anisotropy parameter $c = (\Delta\omega)^{1/2}$ and reduced rotational temperature $Y \equiv kT/B$.

Table 1. For the oblate case at high field, the limit of most interest, the ensemble average reduces simply to

$$\langle\langle\cos^2\theta\rangle\rangle = 1 - (\Delta\omega)^{-1/2} \tag{27}$$

The Legendre expansion is impractical for large $\Delta\omega$ because contributions from the higher terms become large. In that regime, a Gaussian form provides a convenient approximation.[10] For the oblate case, this is

$$\varrho(\theta) = \exp\left(-\frac{1}{2}\sin^2\theta/\sigma^2\right) \tag{28}$$

with the variance given by $\sigma^2 = 1 - \langle\langle\cos^2\theta\rangle\rangle$. The corresponding distribution for the prolate case is $\rho(\theta - \pi/2)$. A chief advantage of the Gaussian form is that it requires only a single quantity, equivalent to just the second Legendre moment. Figure 12 exhibits the dependence of b_2 and $\langle\langle\cos^2\theta\rangle\rangle$ on $\Delta\omega$ and the reduced rotational temperature. This plot enables quick estimates of the ensemble alignment in terms of the rotational temperature, polarizability anisotropy, rotational constant, and laser intensity.

Figure 13 shows typical ensemble-averaged alignment angular distributions. Results obtained from the population-weighted squares of the wave functions, eq 19, are compared with the Gaussian approximation, eq 28. As expected, the Gaussian approximation improves as the distributions become sharper. It thus complements nicely the Legendre expansion, which is very tedious to evaluate for narrow distributions.

5. Applications

Figure 14 provides a nomogram which facilitates estimates of the dimensionless parameters $\Delta\omega$, $\omega_{\parallel}$, and $\omega_{\perp}$ from the polarizability components and the laser field strength. These parameters are related to the polarizability, laser intensity, and rotational constant by

$$\omega \approx 5 \times 10^{12}\alpha[\mathrm{cm}^3]I[\mathrm{W/cm}^2]/B[\mathrm{cm}^{-1}] \tag{29}$$

Available CW infrared lasers combined with buildup cavities can deliver about 10^{11} W/cm^2 at a narrow beam waist. This corresponds to a field strength of about 6×10^6 V/cm, sufficient to induce a dipole moment on the order of 1 D in a typical small molecule such as Cl_2. Pulsed lasers can deliver far higher intensities, although spectroscopic or trapping experiments will usually not want to exceed about 10^{12} W/cm^2 in order to avoid ionizing the molecules. In contrast, only about $\sim 10^5$ V/cm is feasible using a static field. In the nomogram and other illustrative calculations here, we simply use the static polarizability, as the frequency dependence is very weak for nonresonant infrared radiation. Likewise, we neglect even-order hyperpolarizability terms; time-averaging eliminates those of odd order. However, we note that in some applications, it may prove advantageous to use a laser frequency near an infrared-active vibrational fundamental, since then anomalous dispersion will substantially enhance the polarizability and its anisotropy.[11]

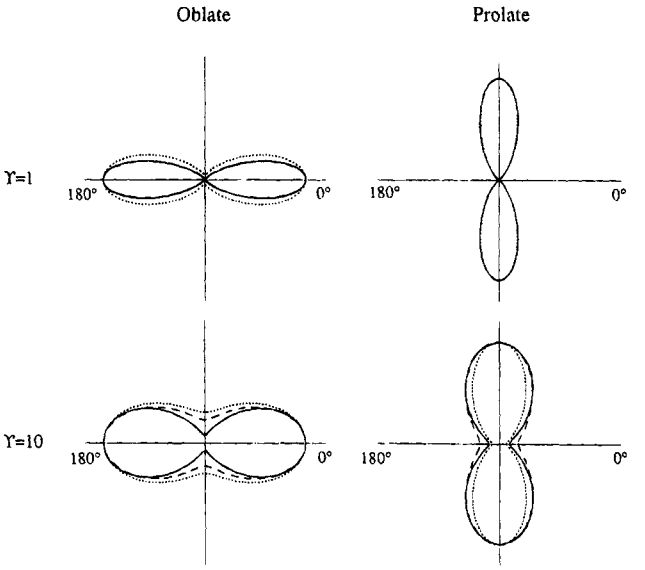

Figure 13. Polar plots of ensemble-averaged alignment angular distributions for the oblate and prolate cases with $|\Delta\omega| = 49$ and reduced rotational temperatures $Y = 1$ and 10. Full curves correspond to exact distributions obtained from the population-weighted squares of the wave functions, eq 19; dashed and dotted curves show Gaussian approximations, eq 28. For the dashed curves, the Gaussian variance was obtained by fitting the exact distribution: $\sigma^2 = 0.90$ and 0.34 at $Y = 1$ and 10, respectively, for the oblate case; $\sigma^2 = 0.09$ and 0.3 at $Y = 1$ and 10 for the prolate case. For the dotted curves, the variance was calculated from $\langle\langle\cos^2\theta\rangle\rangle$ using eq 26: $\sigma^2 = 0.82$ and 0.42 at $Y = 1$ and 10 for the oblate case; $\sigma^2 = 0.09$ and 0.2 at $Y = 1$ and 10 for the prolate case. Legendre series expansion of eq 21 closely matches the exact distributions when terms up to $P_6(\cos\theta)$ are included.

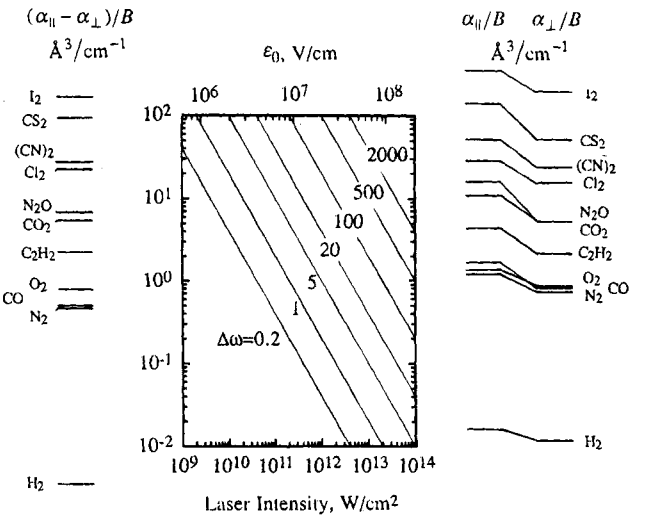

Figure 14. Nomogram for polarizability interaction parameter $\Delta\omega$ of eq 5 as a function of the laser electric field (upper abscissa scale) or intensity (lower scale), and ratio of polarizability anisotropy to rotational constant (left ordinate scale). The nomogram also pertains to the component ratios $\omega_{\parallel}$ and $\omega_{\perp}$ of eq 6 (right scale). Values of the ratios are shown for some typical molecules.

Rotational Spectroscopy of Nonpolar Molecules. Spectral features dependent on the field-induced hybridization of rotational states offer a convenient means to determine the extent

of molecular alignment. These are of particular interest for nonpolar molecules, for which rotational transitions are otherwise not observable. For instance, suppose that, in addition to the laser field that produces the induced dipole moment, the molecule is subjected to weak microwave radiation.[1] Then the rotational transitions can occur with $\Delta J = \pm 2$; by virtue of the hybridization, transitions with $\Delta\tilde{J} = \pm 4, \pm 6, \ldots$ can also occur. The intensities are governed by the square of a matrix element proportional to $\alpha_\perp \epsilon_0 \langle \tilde{J}' | \cos^2 \theta | \tilde{J}'' \rangle$ for $\Delta M = 0$ transitions excited when the microwave radiation is polarized parallel to the laser field and proportional to $\alpha_\parallel \epsilon_0 \langle \tilde{J}' | \sin^2 \theta | \tilde{J}'' \rangle$ for $\Delta M = \pm 2$ transitions excited when polarized perpendicular. For the range of $|M|$ which permits a double-well potential (*cf.* Figure 5), the frequencies of transitions between states that involve tunnel-effect splittings will depend exponentially on $(\alpha_\parallel - \alpha_\perp)\epsilon_0$. Other features of the induced dipole transitions, including the role of nuclear spin statistics, are essentially the same as those for rotational Raman spectra.[12]

For polar molecules aligned by means of the polarizability interaction, spectral transitions involving ordinary electric dipole transitions, with matrix elements governed by $\cos\theta$, will be available in addition to those dependent on the induced dipole moment. However, the hybridization introduces distinctive aspects. Since the $|\tilde{J},|M|;\Delta\omega\rangle$ states are of definite parity (positive for $\tilde{J}$ even and negative for $\tilde{J}$ odd), electric dipole transitions $|\tilde{J}',|M'|;\Delta\omega'\rangle \rightarrow |\tilde{J}'',|M''|;\Delta\omega''\rangle$ can occur only between states with different parities. Also, the hybridization coefficients $d_{J,M}(\Delta\omega)$ of eq 9 give rise to nonzero transition probabilities between states that differ by more than unity in their nominal $\tilde{J}$ values, increasingly so as $\Delta\omega$ increases. Accordingly, the selection rule for electric dipole transitions between pendular states is $\Delta\tilde{J} \equiv \tilde{J}' - \tilde{J}'' = +1, +3, +5, \ldots$, with $\Delta M = 0, \pm 1$ for parallel or perpendicular polarization, as usual.

Anisotropies in Laser-Induced Molecular Dissociation. Striking evidence for alignment by the polarizability interaction has been found in studies of dissociative multiphoton ionization[13,14] of I_2 or CO molecules by intense pulsed infrared lasers ($I \sim 10^{14}$ W/cm^2). The angular distributions of the ionic fragments peak strongly along the direction of the laser polarization. Double-pulse experiments show that this marked anisotropy does not result from orientation dependence of the ionization process, in contrast to photodissociation.[15] The observed anisotropy thus is attributed either to alignment of the molecules prior to dissociation[14] or to the torque exerted on the molecule by the laser field and thereby imparted to the fragments.[13] These are kindred mechanisms, as both depend on the anisotropic polarizability interaction. In a pendular eigenstate, the torque that produced the eigenstate by hybridizing the field-free states is implicitly included in the alignment angular distribution.

Elsewhere we have compared alignment angular distributions[4] computed from eq 28 with observed fragment distributions for the six observed CO dissociative ionization channels.[14] The computed half-widths, obtained simply from $\sin^2 \theta_{1/2} = (2 \ln 2)\sigma^2$, varied from 19° for $\Delta\omega = 4000$ to 53° for $\Delta\omega = 400$, for a reduced temperature $Y = 110$. These widths and the variation with $\Delta\omega$ are at least consistent with the experimental results. A quantitative comparison is precluded because the various decay channels occur in different spatial regions of the focused laser beam, among which the local field intensity varies by perhaps 10-fold or more and is only roughly known.

Table 3 gives a more specific comparison with the I_2 dissociative ionization data.[13] For five channels, both the average peak laser intensity I_0 and the fragment distribution width were reported. (The distributions actually were fitted to $\cos^n \theta$; we converted the reported n values to half-widths via $1/2 = \cos^n \theta_{1/2}$.) From the laser intensities, the rotational constant ($B = 0.03737$ cm^{-1}), and the polarizability anisotropy[16] ($\alpha_\parallel - \alpha_\perp$) = 6.7 Å^3, we find very large values of $\Delta\omega$, ranging from 8.7×10^4 to 3.2×10^4; the reduced temperature is also very large, $Y = 5.6 \times 10^3$. In this regime, the variance parameter σ^2 of eq 28 is simply proportional to $(\Delta\omega)^{-1/2}$. The computed half-widths, including the variation with $\Delta\omega$, agree well with the experimental results. This is gratifying, in view of idealizations in our simplified treatment and in analysis of the experimental data. We find also that both the width and shape given by eq 28 resemble results from detailed calculations[13] that include coupling of electronic states and account explicitly for the torque effects by integrating the equations of motion to map trajectories of the fragment ions.

TABLE 3: Widths of Fragment Angular Distributions from Dissociative Multiphoton Ionization of I_2

channel	laser intensity (10^{14} W/cm^2)	$(\Delta\omega)^{1/2}$	$\theta_{1/2}$ (obs)	$\theta_{1/2}$ (calc)
$I^+ + I^+$	1.0	300	37°	34°
	1.5	360	37°	30°
$I^2 + I^+$	1.8	400	32°	29°
$I^{2+} + I^{2+}$	3.7	570	27°	24°
$I^3 + I^+$	3.7	570	25°	24°

Spatial Trapping of Molecules. Since the polarizability interaction is purely attractive, it offers a means to attain spatial trapping of molecules in a fashion similar to the far-off-resonance technique for atoms.[17] As discussed more fully elsewhere,[4] this appears to be feasible using a CW infrared laser focused to a beam waist of about 10 μm diameter. Within a roughly spherical trapping volume of about 10^{-9} cm^3, the maximum laser field would then exceed 10^{11} W/cm^2, sufficient to provide an attractive potential well with depth on the order of 1 K or more for typical molecular polarizabilities. For a highly polarizable molecule such as the cesium dimer (with $\alpha \sim 130$ Å^3), the well depth would be 150 K; for C_{60} (with $\alpha \sim 83$ Å^3), it would be 60 K. (The polarizability anisotropy has no essential role, other than to enhance the net attractive interaction.) The technique of buffer-gas loading developed for magnetic traps[18] appears well suited to cooling molecules sufficiently to fill a polarizability trap. Estimates[4] of the trap populations attainable for molecules (10^6 molecules at a density of 10^{16} molecules/cm^3) compare favorably with those that have been achieved for atoms.[17]

Acknowledgment. We dedicate this paper to Zdenek Herman in admiration of his zestful science and art. We thank Dr. Paul Corkum (Steacie Institute, Ottawa) for helpful correspondence and Professor John Doyle (Harvard University) for discussions about the trap loading. For support of this and related work, we are grateful to the National Science Foundation.

References and Notes

(1) Townes, C. H.; Schawlow, A. L. *Microwave Spectroscopy*; McGraw-Hill: New York, 1955; pp 270–273.

(2) Loesch, H. J.; Möller, J. *J. Phys. Chem.* **1993**, *97*, 2158 and work cited therein.

(3) Friedrich, B.; Pullman, D.; Herschbach, D. *J. Phys. Chem.* **1991**, *95*, 8118 and work cited therein.

(4) Friedrich, B.; Herschbach, D. *Phys. Rev. Lett.* **1995**, *74*, 4623.

(5) Lowan, A. N. In *Handbook of Mathematical Functions*; Abramowitz, M., Stegun, A., Eds.; Dover: New York, 1972; p 751.

(6) Stratton, J. A.; Morse, P. M.; Chu, L. J.; Little, J. D. C.; Corbató, F. J. *Spheroidal Wave Functions*; Technology Press of MIT: Cambridge, 1956.

(7) Herschbach, D. R.; Loeser, J. G.; Watson, D. K. *Z. Phys. D* **1988**, *10*, 195.

(8) Friedrich, B.; Slenczka, A.; Herschbach, D. *Can. J. Phys.* **1994**, *72*, 897 and work cited therein.

(9) McQuarrie, D. A. *Quantum Chemistry*; University Science Books: Mill Valley, CA, 1983; p 151.

(10) Case, D. A.; Herschbach, D. R. *J. Chem. Phys.* **1976**, *64*, 4212.

(11) Böttcher, C. J. F. *Theory of Electric Polarization*; Elsevier, Amsterdam, 1952.

(12) Herzberg, G. *Spectra of Diatomic Molecules*; Van Nostrand: New York, 1950; pp 88–90.

(13) Dietrich, P.; Strickland, D. T.; Laberge, M.; Corkum, P. B. *Phys. Rev. A* **1993**, *47*, 2305.

(14) Normand, D.; Lompré, L. A.; Cornaggia, C. *J. Phys. B* **1992**, *25*, L497.

(15) Zare, R. N. *Angular Momentum*; Wiley: New York, 1988; pp 120-122.

(16) Callahan, D. W.; Yokozeki, A.; Muenter, J. S. *J. Chem. Phys.* **1980**, *72*, 4791.

(17) Miller, J. D.; Cline, R. A.; Heinzen, D. J. *Phys. Rev. A* **1993**, *47*, R4567.

(18) Doyle, J. M.; Friedrich, B.; Kim, J.; Patterson, D. *Phys. Rev.* A, in press.

JP951785B